exposure to 3,000 p.p.m.. The condensation/vaporization heat of ethanol is larger than that of toluene (42.3 compared to 38.0 kJ mol^{-1} at 298 K) owing to directional interaction in the liquid phase (compare, for example, water), whereas the polymer partitioning of toluene is stronger owing to its higher boiling point. The limits of detection of the calorimetric method are larger than those of the other transducers (40–50 p.p.m. toluene, 100–150 p.p.m. ethanol).

The signals of all three transducers linearly correlate with analyte concentration at low concentrations (less than 3% of saturation vapour pressure at the operating temperature)[13]. As can be seen from the considerable variation in the transducer responses upon gas exposure, different molecular properties or different aspects of the coating–molecule interaction are measured by the different transducers. Alcohols, for example, provide comparably low signals on mass-sensitive transducers owing to their high saturation vapour pressure and low molecular mass, but provide large signals on capacitors owing to their large dielectric constant (24.5). Drastic changes in thermovoltages on the thermopiles are measured for chlorinated hydrocarbons (not shown here) used, for example, in cooling sprays, which in turn have a low dielectric constant, thus showing only small signals on capacitors.

Another powerful feature of the system is that even a zero response from one of the transducers, if there is a measurable response from the other two, is a highly informative data point to help identify the chemical species. To further improve analyte identification/quantification, an array of microsystem chips coated with different polymers could be used.

Our monolithic CMOS gas microsystem is intended to identify organic solvents in transport containers, or to provide information on workplace safety—in, for example, the chemical industry. It will form part of a hand-held or credit-card-sized detection unit. The CMOS approach offers substantial advantages, such as full microelectronics compatibility, extremely small size, low power consumption, and production at industrial standards. We expect that further research and the fast progress of microelectronics development will improve the device performance in the near future. □

1. Massart, D. L., Vandeginste, B. G. M., Deming, S. N., Michotte, Y. & Kaufman, L. *Chemometrics: a Textbook* Vol. 2 (Data Handling in Science and Technology, Elsevier, Amsterdam, 1988).
2. Brereton, R. G. (ed.) *Multivariate Pattern Recognition in Chemometrics* Vol. 9 (Data Handling in Science and Technology, Elsevier, Amsterdam, 1992).
3. Hierlemann, A. *et al.* in *Sensors Update* Vol. 2 (eds Baltes, H., Göpel, W. & Hesse, J.) 119–180 (VCH, Weinheim, 1996).
4. Snow, A. W., Barger, W. R., Klusty, M., Wohltjen, H. & Jarvis, N. L. Simultaneous electrical-conductivity and piezoelectric mass measurements on iodine-doped phthalocyanine Langmuir-Blodgett films. *Langmuir* **2**(4), 513–519 (1986).
5. Rodriguez, J. L., Hughes, R. C., Corbett, W. T. & McWhorter, P. J. in *Technical Digest IEEE International Electron Devices Meeting* 521–524 (IEEE, New York, 1992).
6. Gumbrecht, W. *et al.* Integrated pO_2, pCO_2, pH sensor system for online blood monitoring. *Sensors Actuators B* **18**, 704–708 (1994).
7. Van den Berg, A., van der Waal, P. D., van der Schoot, B. B. & de Rooij, N. F. Silicon-based chemical sensors and chemical analysis systems. *Sensors Materials* **6**, 23–43 (1994).
8. Müller, G., Deimel, P. P., Hellmich, W. & Wagner, C. Sensor fabrication using thin-film-on-silicon approaches. *Thin Solid Films* **296**, 157–163 (1997).
9. Kovacs, G. T. A. *Micromachined Transducers* (WCB McGraw-Hill, Boston, 1998).
10. Madou, M. *Fundamentals of Microfabrication* (CRC, Boca Raton, Florida, 1997).
11. Suehle, J. S., Cavicchi, R. E., Gaitan, M. & Semancik, S. Tin oxide gas sensor fabricated using CMOS micro-hotplates and *in-situ* processing. *IEEE Electron Device Lett.* **14**, 118–120 (1993).
12. Vellekoop, M. J., Lubking, G. W., Sarro, P. M. & Venema, A. Integrated-circuit-compatible design and technology of acoustic-wave-based microsensors. *Sens. Actuators A* **44**, 249–263 (1994).
13. Hierlemann, A., Ricco, A. J., Bodenhöfer, K., Dominik, A. & Göpel, W. Conferring selectivity to chemical sensors via polymer side-chain selection: Thermodynamics of vapor sorption by a set of polysiloxanes on thickness-shear mode resonators. *Anal. Chem.* **72**, 3696–3708 (2000).
14. Koll, A., Kummer, A., Brand, O. & Baltes, H. Discrimination of volatile organic compounds using CMOS capacitive chemical microsensors with thickness-adjusted polymer coating. *Proc. SPIE Smart Struct. Mater.* **3673**, 308–317 (1999).
15. Steiner, F. P. *et al.* in *Digest 8th Int. Conf. on Solid-state Sensors and Actuators* Vol. 2, 814–817 (Foundation for Sensor and Actuator Technology, Stockholm, 1995).
16. Gimzewski, J. K., Gerber, C., Meyer, E. & Schlittler, R. R. Observation of a chemical reaction using a micromechanical sensor. *Chem. Phys. Lett.* **217**, 589–594 (1994).
17. Stowe, T. D. *et al.* Attonewton force detection using ultrathin silicon cantilevers. *Appl. Phys. Lett.* **71**, 288–290 (1997).
18. Lange, D. *et al.* in *Proc. IEEE Workshop on Micro Electro Mechanical Systems (MEMS 99)* 447–452 (IEEE, Piscataway, 1999).
19. Chen, G. Y., Thundat, T., Wachter, E. A. & Warmack, R. J. Adsorption-induced surface stress and its effects on resonance frequency of microcantilevers. *J. Appl. Phys.* **77**, 3618–3622 (1995).
20. Thundat, T., Chen, G. Y., Warmack, R. J., Allison, D. P. & Wachter, E. A. Vapor detection using resonating microcantilevers. *Anal. Chem.* **67**, 519–521 (1995).
21. Lang, H. P. *et al.* A chemical sensor based on a micromechanical cantilever array for the identification of gases. *Appl. Phys. A* **66**, 61–64 (1998).
22. Maute, M. *et al.* Detection of volatile organic compounds with polymer-coated cantilevers. *Sensors Actuators B* **58**, 505–511 (1999).
23. Hagleitner, C., Lange, D., Brand, O., Hierlemann, A. & Baltes, H. in *Digest of Technical Papers IEEE International Solid State Circuits Conf. San Francisco* (ed. Wuorinen, J. H.) Vol. 44, 246 (IEEE, Piscataway, 2001).
24. Bataillard, P., Steffgen, E., Haemmerli, S., Manz, A. & Widmer, H. M. An integrated silicon thermopile as biosensor for the thermal monitoring of glucose, urea and penicillin. *Biosensors Bioelectron.* **8**, 89–98 (1993).
25. Lerchner, J., Seidel, J., Wolf, G. & Weber, E. Calorimetric detection of organic vapors using inclusion reactions with organic coating materials. *Sensors Actuators B* **32**, 71–75 (1996).
26. Van Heerwarden, A. W., Sarro, P. M., Gardner, J. W. & Bataillard, P. Liquid and gas micro-calorimeters for (bio)chemical measurements. *Sensors Actuators A* **43**, 24–30 (1994).
27. Hierlemann, A. *et al.* Application-specific sensor systems based on CMOS chemical microsensors. *Sensors Actuators B* **70**, 2–11 (2000).
28. Koll, A. *et al.* in *Proc. IEEE Workshop on Micro Electro Mechanical Systems (MEMS 99)* 547–551 (IEEE, Piscataway, 1999).
29. Koll, A. *et al.* A flip-chip-packaged CMOS chemical microsystem for detection of volatile organic compounds. *Proc. SPIE Smart Struct. Mater.* **3328**, 223–232 (1998).
30. Ballantine, D. S. *et al. Acoustic Wave Sensors: Theory, Design, and Physico-chemical Applications* (Academic, San Diego, 1997).

··

Formation of coastline features by large-scale instabilities induced by high-angle waves

Andrew Ashton, A. Brad Murray & Olivier Arnault*

Division of Earth and Ocean Sciences/Center for Nonlinear and Complex Systems, Duke University, Box 90227, Durham, North Carolina 27708-0227, USA

···

Alongshore sediment transport that is driven by waves is generally assumed to smooth a coastline. This assumption is valid for small angles between the wave crest lines and the shore, as has been demonstrated in shoreline models[1]. But when the angle between the waves and the shoreline is sufficiently large, small perturbations to a straight shoreline will grow[2,3]. Here we use a numerical model to investigate the implications of this instability mechanism for large-scale morphology over long timescales. Our simulations show growth of coastline perturbations that interact with each other to produce large-scale features that resemble various kinds of natural landforms, including the capes and cuspate forelands observed along the Carolina coast of southeastern North America. Wind and wave data from this area support our hypothesis that such an instability mechanism could be responsible for the formation of shoreline features at spatial scales up to hundreds of kilometres and temporal scales up to millennia.

When waves approach a shore at an oblique angle, nearshore

* Present address: École Normale Supérieure, 45 rue d'ULM, 75005 Paris, France.

wave-breaking produces a shore-parallel current. On a sandy shoreline, this current transports sediment. This alongshore sediment flux, Q_s, is a nonlinear function of the local shoreline angle relative to the wave crests, exhibiting a maximum (Fig. 1a and Methods section). The instability in shoreline shape occurs when waves approach at a relative angle greater than that which maximizes sediment transport (which we will call 'high-angle' waves). In this case, moving alongshore in the transport direction ('downdrift'), Q_s will decrease along the crest of a perturbation as the angle between the shoreline and the waves becomes progressively farther from the transport-maximizing angle (Fig. 1b). This convergence of sediment flux causes accretion; the perturbation will grow. (This conclusion involves the common assumption that the rate of any cross-shore sediment exchange between the nearshore region and deeper water is negligible compared to the alongshore flux.)

Finite-amplitude effects will eventually dictate the evolution of a growing feature. For the case of high-angle waves approaching from a constant direction, as the amplitude of the feature increases, sediment flux at the inflection point downdrift of the crest will approach zero. This will lead to the extension of a spit-like protuberance. In addition, the angle between the shoreline and the wave crests at the inflection point on the updrift side of a feature will approach, but not increase beyond, the angle that maximizes sediment transport. However, the inevitably continued erosion updrift of this point will cause the inflection point to migrate continually towards the crest. This erosion of the updrift flank and accumulation at the crest and downdrift of it will cause the feature to translate downdrift while growing. (If the relative angle between the waves and the regional shoreline trend is only slightly greater than the transport-maximizing angle, subtle, low-amplitude shoreline features will result.)

In the case of multiple shoreline features interacting along an extended shoreline, further morphological evolution resulting from the above-mentioned instability cannot be predicted analytically. To investigate the long-term effect of this instability, we have developed a numerical model. This model is similar to others that discretize a semi-empirical relationship for alongshore sediment flux versus breaking-wave height and angle relative to the shore (Methods)[4,5]. Our model, however, is designed to address morphological evolution on large temporal and spatial scales, and can accommodate arbitrary shoreline shapes (Fig. 2, Methods). It is not designed to simulate the details of any particular geographical location, but to investigate more generally how shorelines might respond to high-angle waves.

In the simplest simulations, waves approach an initially nearly straight shoreline from a constant high angle. With this steady, spatially uniform forcing, the simple, deterministic interactions in the model produce increasingly complex shapes (Fig. 3a). But such simulations omit an important natural condition: varying wave angles. In most simulations, wave angles are distributed according to a probability distribution function (Methods). Features grow for all distributions weighted towards high-angle waves. When the distribution is asymmetric, causing a net sediment flux in one alongshore direction, simulated features translate alongshore (Fig. 3b). In this case, features can overtake each other and merge, and their average wavelength and amplitude increase with time.

Somewhat surprisingly, the wavelength and amplitude of the shoreline forms also continually increase for the case of a symmetric wave distribution (Fig. 3c). Simulations reveal that slightly larger features shelter their neighbours from the highest-angle waves, causing the larger features to grow relative to the smaller features, increasing the sheltering effect. The smaller features will eventually experience a wave distribution weighted towards low-angle waves, resulting in the rapid disappearance of the smaller features and growth of their neighbours. As the features develop, the wave
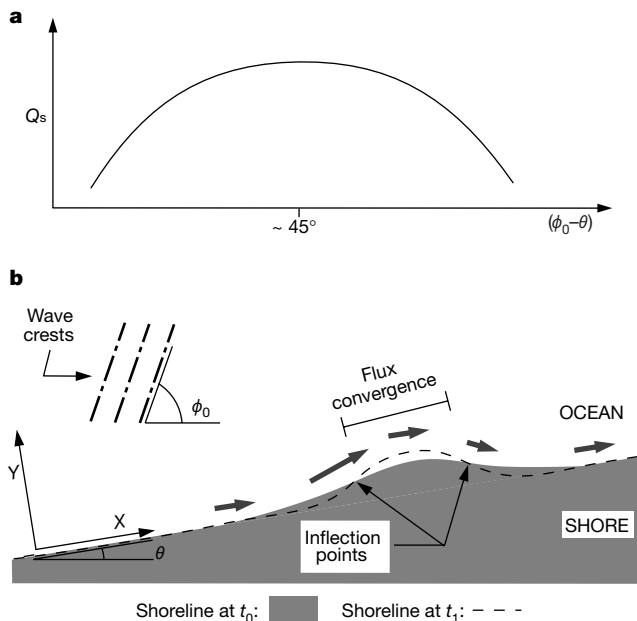
Figure 1 As a result of the basic instability, shoreline perturbations grow in the presence of high-angle waves. **a**, Schematic relationship between alongshore sediment flux, Q_s, and the relative angle between wave crests in deep water (before nearshore refraction), ϕ_0, and the local shoreline orientation, θ, showing a maximum for $\phi_0 - \theta \approx 45°$. **b**, The relative magnitude of the alongshore sediment flux, shown by the length of the arrows, and the consequent zones of erosion and accretion on a perturbation to a straight shoreline when the angle between the wave crests and the shoreline trend is greater than that which maximizes the sediment flux.
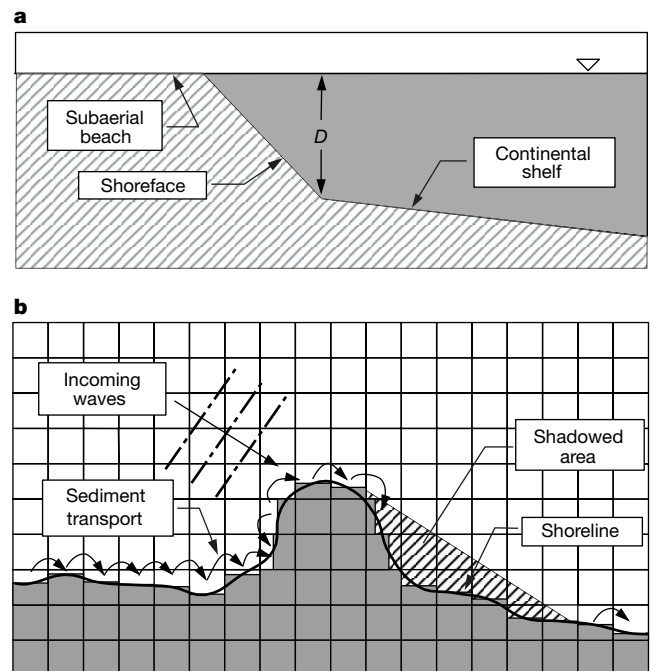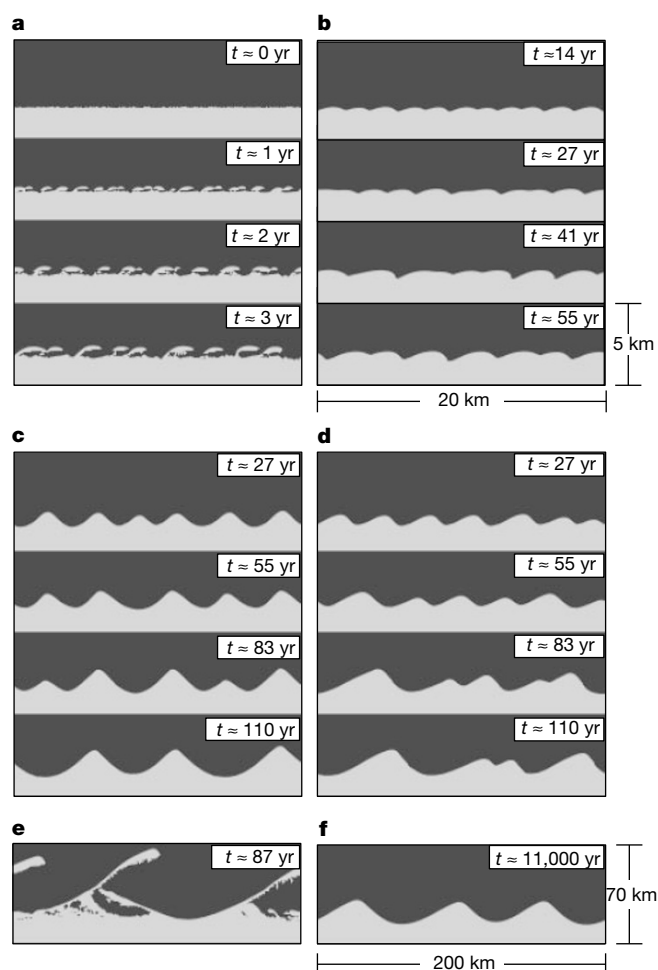

Figure 2 Schematic illustration of the model algorithm. This algorithm, described in Methods, allows the treatment of an arbitrarily complex shoreline. **a**, Profile in the cross-shore direction showing D, the depth at which cross-shore transport is considered negligible, defined as the intersection of the continental shelf with the shoreface, with an imposed minimum depth. The inverted triangle indicates sea level. **b**, Plan view showing the direction of sediment transport between discretized shoreline cells for waves approaching at a given angle. Also shown is the region of the shoreline 'shadowed' from the incoming waves; no sediment is transported between cells in this area.

climate along the flanks also becomes low angle; the evolution of large-scale features inhibits the growth of smaller-scale perturbations (Fig. 3c). Simulations with a slightly asymmetric wave-angle distribution exhibit both forms of behaviour (Fig. 3d).

With greater wave asymmetry and a strong predominance of high-angle waves, large spits extend offshore, and they shelter a downdrift region from waves coming from the dominant direction. Perturbations will then grow in this shadowed area that migrate in a direction opposite to the regional alongshore drift and eventually merge with the larger spit (Fig. 3e).
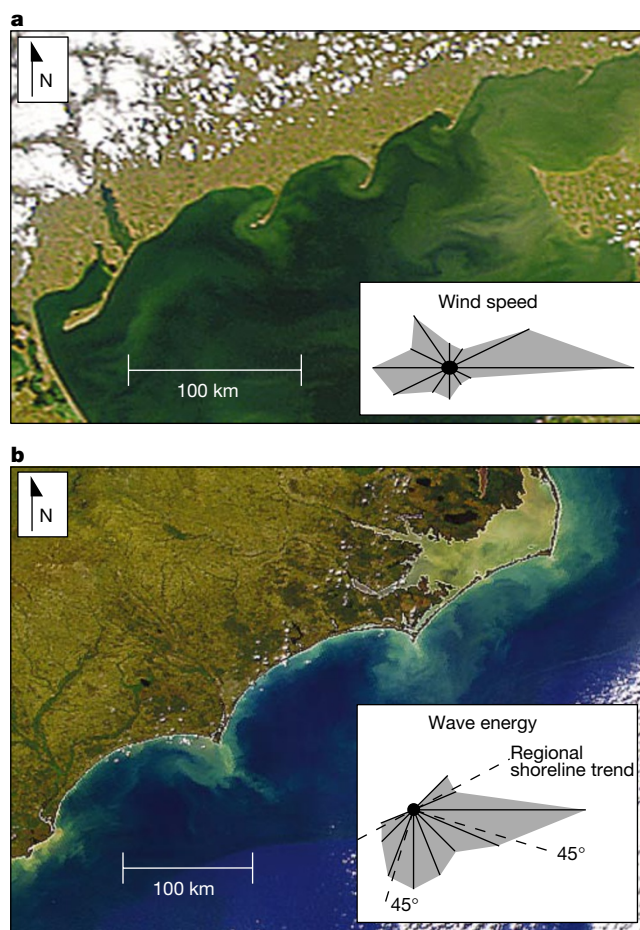
In simulations with highly asymmetric wave distributions, simulated features resemble a class of shoreline phenomena given various names, including 'cuspate spits'[2,6], 'sandwaves'[7–11], 'ords'[12], and 'humps'[13]. On some open ocean coasts, these can be subtle, migrating, spatially correlated zones of accretion alternating with erosion 'hot spots'[7,8,10,13]. Pronounced spit- or wave-shaped shoreline features exist in many elongate water bodies, such as the Great Lakes[14], the Sea of Azov[2] (Fig. 4a) and some back-barrier lagoons[2,6]. In these water bodies, most of the large waves are generated across the larger fetch along the long axis; even isotropically distributed winds will result in a dominance of high-angle waves.

With a symmetric or slightly asymmetric wave distribution in the model, simulated features resemble 'cuspate forelands'[15,16] or 'v-notches'[17] found in nature. After a simulated time of the order of 10^4 years (with a constant offshore wave height of 2 m and wave period of 5 s), the cuspate pattern develops a length scale of the order of 100 km (Fig. 3f), commensurate with some of the largest cuspate forelands found in nature.

The capes of the North Carolina coast of North America provide the most dramatic example of this phenomenon (Fig. 4b). Many hypotheses for the origin of these capes have been suggested, most involving external templates such as ancient river deltas[18,19]. However, estimates of the modern wave climate off the Outer Banks of North Carolina suggest that a predominance of the wave energy comes from high angles (Fig. 4b)[20]. Although these estimates do not conclusively establish the regional wave climate, and do not necessarily reflect previous wave conditions, they are consistent with the hypothesis that the large-scale pattern of this coastline has emerged spontaneously, driven by the instability inherent in the

Figure 3 Plan views of the model domain, showing the shoreline evolution. Cell width is 100 m (except where noted). **a**, Results using a single angle (55°) between deep-water wave crests and the global shoreline orientation. **b**, Results when the distribution of deep-water wave angles is weighted towards high angles and towards waves approaching from the left. In this simulation, $\alpha = 0.8$ and $\beta = 0.8$ (see Methods). **c**, Results with a wave distribution weighted toward high angles ($\alpha = 0.6$), but with waves symmetrically distributed from left and right ($\beta = 0.5$). **d**, Slight asymmetry ($\alpha = 0.7$, $\beta = 0.6$). **e**, Longer-term evolution of a cuspate spit ($\alpha = 0.6$, $\beta = 0.7$). **f**, Results for $\alpha = 0.7$ and $\beta = 0.57$, with cell width representing 1 km.

Figure 4 Satellite images showing naturally occurring large-scale shoreline features. **a**, The Sea of Azov, Ukraine, with (inset) directionally binned 'rose' of wind speed showing a dominance of winds from the east. Wind data (from NOAA National Climate Data Centre, Ashville, North Carolina) from 1991–2001 at meteorological station 34712, in Mariupol', on the north shore of the Sea of Azov. **b**, The Carolina coast, USA, with (inset) directionally binned WIS hindcast of wave energy (estimated from meteorological data, solid lines) plotted against the shoreline trend (defined by the backs of the bays, dashed line)[20]. The relatively large amount of energy approaching from directions between the shoreline trend and 45° to it indicates the predominance of waves with high angles between wave crests and the shoreline trend. Data represent the period 1976–95, at station 52 in 22 m water depth off Cape Hatteras. Neighbouring stations in 27–35 m water depth show a similar distribution. Satellite images courtesy of the SeaWiFS Project NASA/GSFC and ORBIMAGE.

relationship between alongshore sediment transport and local shoreline orientation.

Sea level has remained near its current high elevation (relative to the elevations during Pleistocene glaciations) only of the order of 10^3 years, rather than the 10^4 years required in the model for 100-kilometre-scale features to develop. However, the Carolina capes could have continued to develop over several sea-level high stands; the rapidly rising sea level early in interglacial periods could have encountered abandoned variegated shorelines that evolved during a previous high stand. (Preserved shorelines on the North Carolina coastal plain suggest cape development during Pleistocene times[21].) Our initial model does not explicitly include sea-level rise or the dynamics of barrier islands. However, during the relatively slow sea-level rise of recent millennia, the development of large-scale shoreline shapes could have been superimposed on the general trend of shoreline regression.

The assumptions used to develop the numerical model are specifically applicable to large spatial and temporal scales. The magnitude of these scales depends on wave height and period (which influence the scale of the alongshore current and the depth to which transport is active). On open-ocean coasts, the model assumptions do not hold for shoreline changes on scales smaller than kilometres and decades. However, during storms producing locally high-angle waves, the fundamental instability would still operate. The resulting spatially isolated zones of erosion could make a shoreline's response to storms more complex than might naively be expected. Some of the transient erosion 'hot spots' that occur along some shorelines after large storms[22,23] could possibly be related to this instability. Natural shorelines include complicated cross-shore and alongshore bathymetry, and other processes that can produce localized zones of erosion, such as rip currents. However, the recently documented patterns of erosion and accretion exhibit alongshore scales including that of several kilometres[22], and a power-law scaling indicating changes on all spatial scales over a broad range[24]. These observations are inconsistent with a rip-current origin, but this behaviour occurring across a range of scales could be explained by the basic instability in alongshore sediment transport.

This simplified, initial numerical model is limited in several other ways. It applies not to predominantly rocky coasts, but only to shorelines that remain covered with at least a veneer of mobile sediment, even in areas where the shoreline is eroding. If weathering of intermittently exposed rocks on the nearshore bed (the 'shoreface') does not occur as rapidly as sediment is removed, or if the eroding shoreface rocks are composed partly of fine-grained material that does not remain in the nearshore system, the resulting geometry of the shapes will be affected. But none of these processes would counteract the fundamental instability being investigated.

We have also intentionally omitted several other natural phenomena, including: (1) alongshore inhomogeneities, such as variations in grain size and lithology; (2) wave diffraction; (3) the convergence and divergence of wave rays that tends to concentrate wave energy on headlands and away from bays; and (4) the residual motion that arises when tidal currents pass a headland. This last process can transport sediment off a cape onto a subaqueous shoal, acting as a sediment sink that can influence cape dynamics and morphology[25].

In this initial numerical exploration, our goal has not been to reproduce any natural system in detail, or to create a maximally accurate model, but rather to investigate the range of coastal landforms and behaviours that could result from the fundamental instability in alongshore sediment transport that occurs in regions with predominantly high-angle waves. The numerical model indicates that this instability could be responsible for the self-organization of a wide variety of well documented but poorly understood shoreline phenomena. □

Methods

Sediment transport

The flux of alongshore momentum that waves carry towards the shore, termed the alongshore 'thrust'[26], drives an alongshore current and sediment transport. If the relative angle between the waves and the shoreline ($\phi_0 - \theta$) approaches zero, the component of the wave-momentum flux in the alongshore direction approaches zero. If the relative wave angle approaches 90°, then the rate at which wave momentum and energy are transported towards the shore approaches zero. Between these extremes, the thrust reaches a maximum. A well-known semi-empirical formula for Q_s can be expressed in terms of this thrust multiplied by the breaking-wave celerity[27,28]. Assuming both refraction over shore-parallel contours and no dissipation of wave energy, the thrust is constant outside the surf zone[28], so that this formula can be written either in terms of breaking-wave properties or in terms of deep-water quantities: $Q_s = K H_b^{5/2} \sin(\phi_b - \theta) \cos(\phi_b - \theta) = K H_b^{1/2} H_0^2 \sin(\phi_0 - \theta) \cos(\phi_0 - \theta) \approx K_2 H_0^{12/5} \sin(\phi_0 - \theta) \cos^{6/5}(\phi_0 - \theta)$, where H is the wave height, K and K_2 are constants and the subscripts b and 0 refer to breaking- and deep-water values, respectively. The deep-water form predicts a maximum in sediment transport for offshore waves approaching the local shoreline at an angle of approximately 42°. An analysis[29] of surf-zone processes predicts a very similar curve, with Q_s maximized for a relative offshore wave angle slightly greater than 45°. (In the more familiar breaking-wave formula, with H_b held constant, sediment transport is maximized for $\phi_b - \theta = 45°$. However, with H_0 and ϕ_0 held constant, higher values of $\phi_b - \theta$ are associated with greater nearshore refraction, which tends to reduce H_b. As an example, if $H_0 = 2$ m, wave period is 10 s, and assuming shore-parallel contours, sediment transport is maximized for $\phi_b - \theta \approx 10°$.)

Model

The model divides the plan-view domain into cells that are filled with a fractional amount of sediment, F_i. Cells with $F_i = 1$ form the subaerial coast, and cells adjacent to these with $0 < F_i < 1$ constitute the shoreline, with F_i representing the fractional position of the shoreline within the cell. For each boundary between shoreline cells, the sign of the angle between deep-water wave crests and the line connecting the shoreline positions in adjacent shoreline cells determines the direction of alongshore sediment transport between the neighbouring cells. To avoid discretization artefacts (for the case of high-angle waves), we use a scheme that combines upwind and central finite-difference techniques: if the magnitude of the local relative wave angle—defined using the position of the shoreline in cells bounding the cell sediment transport is from—is less than (greater than) that which maximizes the transport, we use a central (upwind) finite-difference technique to determine the sediment flux. When moving from a boundary with central differencing to one with upwind differencing, sediment transport for the latter boundary is set to that occurring for $\phi_b - \theta = 45°$, with the local H_b. Sediment is not transported out of cells that are 'shadowed' from incoming waves by other portions of the shoreline (Fig. 2b). Sediment transport into a shadowed region is calculated using an upwind finite-difference.

Sediment flux is determined using $Q_s = K H_b^{5/2} \sin(\phi_b - \theta) \cos(\phi_b - \theta)$, where $K = 6.4 \times 10^4$ m^3 d^{-1} is used for all simulations[1]. (Deep-water wave heights and angles are converted to breaking-wave quantities using linear-wave theory for shoaling and refraction over shore-parallel contours, and assuming depth-limited breaking.) Fractional sediment contents of shoreline cells are adjusted according to the net sediment flux into or out of the cell, $Q_{s,\text{net}}$: $\Delta F_i = Q_{s,\text{net}} \Delta t / (W^2 D_i)$, where W is the horizontal cell width and D_i represents the depth to which profile accumulation or erosion extends (below which cross-shore transport is considered negligible). D_i is defined in the model as the intersection of the continental shelf (which has a slope $S_{cs} = 0.001$, perpendicular to the global shoreline trend) with a linear nearshore profile (representing the 'shoreface', which has a slope $S_{sf} = 0.01$, extending from the subaerial portion of the beach in a direction perpendicular to the local shoreline orientation). Imposing a minimum depth, D_{min}, represents the erosion of the shoreface by wave action where the shore moves landward.

In each simulation, the initial conditions consist of a straight shoreline (at an average of 9,000 m seaward of the intersection of the projection of the continental shelf slope and sea level), plus uncorrelated random, white-noise perturbations to the shoreline position in each shoreline cell, with an amplitude of one cell width. When deep-water wave angles are varied during model runs, each simulated day, (1) a random number between 0 and 1, X, is chosen, and the deep-water wave angle is determined by $\phi_0 = (4\pi/9)X^\alpha$, where α is a set parameter; and (2) a different random number between 0 and 1, Y, is chosen, and sign of the wave angle is positive if $Y > \beta$ and negative if $Y < \beta$ (positive is from the left, negative from the right), where β is a set parameter between 0 and 1.

1. Komar, P. D. *Beach Processes and Sedimentation* (Simon & Schuster, Upper Saddle River, New Jersey, 1998).
2. Zenkovitch, V. P. On the genesis of cuspate spits along lagoon shores. *J. Geol.* **67,** 269–277 (1959).
3. Wang, J. D. & Le Mehaute, B. in *Proc. 17th Coastal Eng. Conf.* 1295–1305 (American Society of Civil Engineers, New York, 1980).
4. Hanson, H. & Kraus, N. C. *GENESIS: Generalized Model for Simulating Shoreline Change, Report 1: Technical Reference* (US Army Eng. Waterways Experiment Station, Coastal Eng. Res. Cent., Vicksburg, Mississippi, 1989).
5. Le Mehaute, B. & Soldate, M. in *Proc. 16th Coastal Eng. Conf.* 1163–1179 (American Society of Civil Engineers, New York, 1979).
6. Fisher, R. L. Cuspate spits of Saint Lawrence Island, Alaska. *J. Geol.* **63,** 133–142 (1955).
7. Bruun, P. in *Proc. 5th Conf. on Coastal Eng.* 269–295 (American Society of Civil Engineers, New York, 1954).
8. Bakker, W. T. A mathematical theory about sandwaves and its applications on the Dutch Wadden Isle of Vlieland. *Shore Beach* **36,** 4–14 (1968).

9. Sonu, C. J. in *Proc. 11th Conf. on Coastal Eng.* Vol. 1, 373–400 (American Society of Civil Engineers, New York, 1969).
10. Verhagen, H. J. Sand waves along the Dutch coast. *Coastal Eng.* **13,** 129–147 (1989).
11. Thevenot, M. M. & Kraus, N. C. Longshore and sand waves at Southampton Beach, New York: observation and numerical simulation of their movement. *Mar. Geol.* **126,** 249–269 (1995).
12. Pringle, A. W. Holderness coast erosion and the significance of ords. *Earth Surf. Processes Landforms* **10,** 107–124 (1985).
13. Inman, D. L. Accretion and erosion waves on beaches. *Shore Beach* **55,** 61–66 (1987).
14. Stewart, C. J. & Davidson-Arnott, R. G. D. Morphology, formation and migration of longshore sandwaves; Long Point, Lake Erie, Canada. *Mar. Geol.* **81,** 63–77 (1988).
15. Gulliver, F. P. Cuspate forelands. *Geol. Soc. Am. Bull.* **7,** 399–422 (1896).
16. Wilson, A. W. G. Cuspate forelands along the Bay of Quinte. *J. Geol.* **12,** 106–132 (1904).
17. Gilbert, G. K. The topographic features of lake shores. *US Geol. Surv. Ann. Rep.* **5,** 69–123 (1885).
18. Hoyt, J. H. & Henry, V. J. Origin of capes and shoals along the southeastern coast of the United States. *Geol. Soc. Am. Bull.* **82,** 59–66 (1971).
19. White, W. A. Drainage symmetry and the Carolina Capes. *Geol. Soc. Am. Bull.* **77,** 223–240 (1966).
20. US Army Corps of Engineers *Wave Information Study* at ⟨http://bigfoot.wes.army.mil/u003.html⟩ (2001).
21. Moslow, T. F. & Heron, S. D. Holocene depositional history of a microtidal cuspate foreland cape: Cape Lookout, North Carolina. *Mar. Geol.* **41,** 251–270 (1981).
22. List, J. & Farris, A. F. in *Coastal Sediments '99* (eds Drause, N. C. & McLougal, W. G.) 1324–1338 (American Society of Civil Engineers, Long Island, 1999).
23. Stockdon, H. F., Holman, R. A. & Sallenger, A. H. Longshore variability of the coastal response to extreme storms. *Eos* **81,** F673 (2000).
24. Tebbens, S. F. & Nelson, E. Wavelet analysis of shoreline change at Cape Hatteras National Seashore. *Eos* **81,** F562 (2000).
25. McNinch, J. E. & Luettich, R. A. Physical processes around a cuspate foreland headland: implications to the evolution and long-term maintenance of a cape-associated shoal. *Continental Shelf Res.* **20,** 2367–2389 (2000).
26. Longuet-Higgins, M. S. Longshore currents generated by obliquely incident waves, 1. *J. Geophys. Res.* **75,** 6778–6789 (1970).
27. Komar, P. D. & Inman, D. L. Longshore sand transport on beaches. *J. Geophys. Res.* **75,** 5914–5927 (1970).
28. Longuet-Higgins, M. S. in *Waves on Beaches and Resulting Sediment Transport* (ed. Meyer, R. E.) 373–400 (Academic, New York, 1972).
29. Deigaard, R., Fredsoe, J. & Hedegaard, I. B. Mathematical model for littoral drift. *J. Waterway Port Coast. Ocean Eng.* **112,** 351–369 (1988).

....

Female sticklebacks count alleles in a strategy of sexual selection explaining MHC polymorphism

Thorsten B. H. Reusch*†, **Michael A. Häberli***†. **Peter B. Aeschlimann***†
& Manfred Milinski*

* *Max Planck Institute for Limnology, Department of Evolutionary Ecology,*
Postfach 165, 24306 Plön, Germany
† *These authors contributed equally to this work*

...

The origin and maintenance of polymorphism in major histocompatibility complex (MHC) genes in natural populations is still unresolved[1]. Sexual selection, frequency-dependent selection by parasites and pathogens, and heterozygote advantage have been suggested to explain the maintenance of high allele diversity at MHC genes[2–4]. Here we argue that there are two (non-exclusive) strategies for MHC-related sexual selection, representing solutions to two different problems: inbreeding avoidance and parasite resistance. In species prone to inadvertent inbreeding, partners should prefer dissimilar MHC genotypes to similar ones. But if the goal is to maximize the resistance of offspring towards potential infections, the choosing sex should prefer mates with a higher diversity of MHC alleles. This latter strategy should apply when there are several MHC loci, as is the case in most vertebrates[2,5]. We tested the relative importance of an 'allele count-

ing' strategy compared to a disassortative mating strategy using wild-caught three-spined sticklebacks (*Gasterosteus aculeatus*) from an interconnected system of lakes. Here we show that gravid female fish preferred the odour of males with a large number of MHC class-IIB alleles to that of males with fewer alleles. Females did not prefer male genotypes dissimilar to their own.

Sexual selection, the preference of certain mating partners over others, is ubiquitous among animals[6,7]. The choosing sex may be able to increase the attractiveness of offspring, or gain direct benefits such as parental care[8]. Another function of mate choice is to increase the fitness of offspring by either choosing 'good genes', or avoiding incompatible 'bad genes'—for example in matings with close kin. Particularly suited for testing the idea of choosiness with respect to genes is the MHC, a multigene family that is important in controlling the vertebrate immune system by presentation of self and foreign peptides to T cells[2]. MHC alleles confer specific resistance against pathogens and parasites. Therefore, mate choice should increase the fitness of offspring by maximizing the heterozygosity at MHC loci[1,4,9,10], allowing a wider spectrum of pathogens to be recognized during early infection.

The focus of previous studies was disassortative mating, that is, the preference of dissimilar males or females as a mating partner[11–13], as a means of inbreeding avoidance, or in order to increase the heterozygosity at MHC loci[3,14]. In the context of sexual selection, it has not been taken into account that most vertebrates possess several MHC loci[5]. As a result, there are many possible combinations of alleles at different loci[2]. The chances of choosing a partner with identical MHC haplotypes become very unlikely because the combination of alleles at multiple loci renders the expected likelihood of existing MHC genotypes very small, even under linkage disequilibrium. A mechanism of sexual selection focusing on the distinction between similar and dissimilar MHC genotypes becomes inefficient when increasing parasite resistance is important. Females should rather choose partners that maximize the number of different MHC alleles in their offspring[3].

We studied populations of the three-spined stickleback (*Gasterosteus aculeatus*) where we identified high MHC diversity for partial sequences of MHC class-IIB loci, coding for the peptide-binding region. At an estimated six loci[15], we identified 24 distinct sequences in only eight fish from a system of interconnected populations, and many more alleles were identified on the basis of single-strand conformation polymorphisms (SSCP) in a total of 144 fish. We also observed marked differences in the number of different alleles per individual fish, varying between two and eight detectable alleles across all loci (Fig. 1). For one location (Schöhsee) we calculated that the chance a female has of mating with an MHC-identical male is only 1% if she mates at random. But the probability of choosing a mate with fewer alleles is 46% under random expectations (see Methods). Therefore, we predicted that females
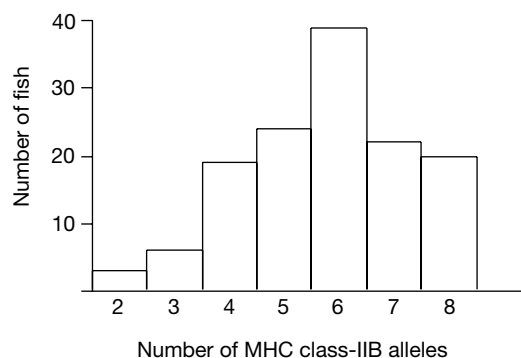
Figure 1 Frequency distribution of the number of MHC class-IIB alleles (peptide-binding region) detectable by SSCP in 144 fish from one population (Schöhsee). The mean number of MHC alleles ± s.e. was 5.8 ± 0.13.

letters to nature

Methods

Protein purification and crystallization

We prepared RanGAP from *Schizosaccharomyces pombe* and human Ran as described. Human RanBP1 was expressed in BL21 *Escherichia coli* as a glutathione *S*-transferase fusion protein and subsequently purified with Glutathione–Sepharose 4 Fast Flow (Amersham Pharmacia). We loaded RanBP1 onto an affinity column and added Ran–GppNHp in twofold excess afterwards. The binary complex was eluted after a 12-h incubation with thrombin protease. We then added RanGAP in excess and purified the ternary complex by size-exclusion chromatography in buffer (20 mM Tris-HCl pH 7.5, 2 mM MgCl$_2$, 2 mM dithioerythritol (DTE)). Crystals were grown by hanging drop from 18.5–20.5% PEG4000, 100 mM potassium acetate, 100 mM Tris-HCl pH 7.5 for the GppNHp complex. After 3–4 d at 20 °C, thin needle protein crystals appeared (500 × 45 × 45 μm^3).

For the transition-state analogue complex, RanBP1, Ran–GDP and RanGAP were mixed in a buffer containing 2 mM Al^{3+} and 30 mM NaF. Subsequently, the ternary complex was purified by size-exclusion chromatography in 20 mM Tris-HCl pH 7.5, 2 mM MgCl$_2$, 2 mM DTE containing additional 30 mM NaF. Crystals were grown from 18.5–20.5% PEG4000, 100 mM Tris-HCl pH 7.5 at 20 °C.

Data collection and structure determination

The crystals, with space group *P*1 and unit-cell dimensions of *a* = 101.6 Å, *b* = 103.1 Å, *c* = 120.2 Å, α = 71.6, β = 80.6, γ = 67.8, were very sensitive to radiation damage. Data sets were obtained by translating a single crystal needle and successively exposing small sections to the beam. Data were collected on MAR image plate detectors at the beam lines ID13 and ID14-1 (for AlF$_x$) at the European Synchrotron Radiation Facility (ESRF) and were processed with DENZO[27]. We solved the structure of the complex by molecular replacement using AMORE[28] with RanGAP[7] as a model (correlation coefficient 0.41, *R*-factor 0.47). The initial electron density was improved greatly by four-fold averaging using the non-crystallographic symmetry (NCS) in the unit cell. After inclusion of Ran and RanGAP the DM[28] correlation coefficient for the RanBP1 electron density was 0.77. The model of the ternary complex was built using the program O[29] and refined with CNS applying NCS restraints[30]. The final model comprises residues 2–345 of RanGAP, 8–213 of Ran and 22–167 of RanBP1.

Received 9 August; accepted 29 November 2001.

1. Scheffzek, K. *et al.* The Ras-RasGAP complex: structural basis for GTPase activation and its loss in oncogenic Ras mutants. *Science* **277,** 333–338 (1997).
2. Rittinger, K. *et al.* Structure at 1.65 Å of RhoA and its GTPase-activating protein in complex with a transition-state analogue. *Nature* **389,** 758–762 (1997).
3. Görlich, D. & Kutay, U. Transport between the cell nucleus and the cytoplasm. *Annu. Rev. Cell Dev. Biol.* **15,** 607–660 (1999).
4. Bischoff, F. R., Krebber, H., Smirnova, E., Dong, W. & Ponstingl, H. Co-activation of RanGTPase and inhibition of GTP dissociation by Ran-GTP binding protein RanBP1. *EMBO J.* **14,** 705–715 (1995).
5. Bischoff, F. R. & Görlich, D. RanBP1 is crucial for the release of RanGTP from importin beta-related nuclear transport factors. *FEBS Lett.* **419,** 249–254 (1997).
6. Becker, J. *et al.* RNA1 encodes a GTPase-activating protein specific for Gsp1p, the Ran/TC4 homologue of *Saccharomyces cerevisiae. J. Biol. Chem.* **270,** 11860–11865 (1995).
7. Hillig, R. C. *et al.* The crystal structure of rna1p: a new fold for a GTPase-activating protein. *Mol. Cell.* **3,** 781–791 (1999).
8. Vetter, I. R., Arndt, A., Kutay, U., Görlich, D. & Wittinghofer, A. Structural view of the Ran-Importin β interaction at 2.3 Å resolution. *Cell* **97,** 635–646 (1999).
9. Chook, Y. M. & Blobel, G. Structure of the nuclear transport complex karyopherin-β2-Ran.GppNHp. *Nature* **399,** 230–237 (1999).
10. Haberland, J., Becker, J. & Gerke, V. The acidic C-terminal domain of rna1p is required for the binding of Ran.GTP and for RanGAP activity. *J. Biol. Chem.* **272,** 24717–24726 (1997).
11. Lounsbury, K. M., Richards, S. A., Carey, K. L. & Macara, I. G. Mutations within the Ran/TC4 GTPase. Effects on regulatory factor interactions and subcellular localization. *J. Biol. Chem.* **271,** 32834–32841 (1996).
12. Vetter, I. R., Nowak, C., Nishimoto, T., Kuhlmann, J. & Wittinghofer, A. Structure of a Ran-binding domain complexed with Ran bound to a GTP analogue: implications for nuclear transport. *Nature* **398,** 39–46 (1999).
13. Richards, S. A., Lounsbury, K. M. & Macara, I. G. The C terminus of the nuclear RAN/TC4 GTPase stabilizes the GDP-bound state and mediates interactions with RCC1, RAN-GAP, and HTF9A/RANBP1. *J. Biol. Chem.* **270,** 14405–14411 (1995).
14. Scheffzek, K., Klebe, C., Fritz-Wolf, K., Kabsch, W. & Wittinghofer, A. Crystal structure of the nuclear Ras-related protein Ran in its GDP-bound form. *Nature* **374,** 378–381 (1995).
15. Haberland, J. & Gerke, V. Conserved charged residues in the leucine-rich repeat domain of the Ran GTPase activating protein are required for Ran binding and GTPase activation. *Biochem. J.* **343,** 653–662 (1999).
16. Nassar, N., Hoffman, G. R., Manor, D., Clardy, J. C. & Cerione, R. A. Structures of Cdc42 bound to the active and catalytically compromised forms of Cdc42GAP. *Nature Struct. Biol.* **5,** 1047–1052 (1998).
17. Tesmer, J. J., Berman, D. M., Gilman, A. G. & Sprang, S. R. Structure of RGS4 bound to AlF4⁻-activated G$_{iα1}$: stabilization of the transition state for GTP hydrolysis. *Cell* **89,** 251–261 (1997).
18. Der, C. J., Finkel, T. & Cooper, G. M. Biological and biochemical properties of human rasH genes mutated at codon 61. *Cell* **44,** 167–176 (1986).
19. Klebe, C., Bischoff, F. R., Ponstingl, H. & Wittinghofer, A. Interaction of the nuclear GTP-binding protein Ran with its regulatory proteins RCC1 and RanGAP1. *Biochemistry* **34,** 639–647 (1995).
20. Albert, S., Will, E. & Gallwitz, D. Identification of the catalytic domains and their functionally critical arginine residues of two yeast GTPase-activating proteins specific for Ypt/Rab transport GTPases. *EMBO J.* **18,** 5216–5225 (1999).
21. Ahmadian, M. R., Stege, P., Scheffzek, K. & Wittinghofer, A. Confirmation of the arginine-finger hypothesis for the GAP-stimulated GTP-hydrolysis reaction of Ras. *Nature Struct. Biol.* **4,** 686–689 (1997).
22. Graham, D. L., Eccleston, J. F. & Lowe, P. N. The conserved arginine in rho-GTPase-activating protein is essential for efficient catalysis but not for complex formation with Rho.GDP and aluminium fluoride. *Biochemistry* **38,** 985–991 (1999).
23. Berman, D. M., Wilkie, T. M. & Gilman, A. G. GAIP and RGS4 are GTPase-activating proteins for the G$_i$ subfamily of G protein α subunits. *Cell* **86,** 445–452 (1996).
24. Maegley, K. A., Admiraal, S. J. & Herschlag, D. Ras-catalyzed hydrolysis of GTP: a new perspective from model studies. *Proc. Natl Acad. Sci. USA* **93,** 8160–8166 (1996).
25. Allin, C., Ahmadian, M. R., Wittinghofer, A. & Gerwert, K. Monitoring the GAP catalyzed H-Ras GTPase reaction at atomic resolution in real time. *Proc. Natl Acad. Sci. USA* **98,** 7754–7759 (2001).
26. Prakash, B., Renault, L., Praefcke, G. J., Herrmann, C. & Wittinghofer, A. Triphosphate structure of guanylate-binding protein 1 and implications for nucleotide binding and GTPase mechanism. *EMBO J.* **19,** 4555–4564 (2000).
27. Otwinowski, Z. & Minor, W. Processing of X-ray diffraction data collected in oscillation mode. *Methods Enzymol.* **276,** 307–326 (1997).
28. Collaborative Computational Project No. 4. The CCP4 suite: programs for protein crystallography. *Acta Crystallogr. D* **50,** 760–763 (1994).
29. Jones, T. A. & Kjeldgaard, M. Electron-density map interpretation. *Methods Enzymol.* **277,** 173–208 (1997).
30. Brunger, A. T. *et al.* Crystallography and NMR system (CNS): A new software system for macromolecular structure determination. *Acta Crystallogr. D* **54,** 905–921 (1998).

●●

erratum

Formation of coastline features by large-scale instabilities induced by high-angle waves

Andrew Ashton, A. Brad Murray & Olivier Arnoult

Nature **414,** 296–300 (2001).

In this Letter, the last name of the third author, Olivier Arnoult, was misspelled as 'Arnault'. ☐